Optimized Current Regulator Design for *LCL*-Filtered Inverters Exposed to Weak Grids

Jack S. Bryant,[1] Brendan McGrath,[2] Lasantha Meegahapola,[2] and Peter Sokolowski[3]
jack@amperelabs.com.au, {brendan.mcgrath, lasantha.meegahapola}@rmit.edu.au
[1]Ampere Labs, Murdoch, WA, Australia
[2]School of Engineering, RMIT University, Melbourne, VIC, Australia
[3]No current affiliation

***Abstract*—Grid-feeding inverter instability is prevalent in weak grid conditions where the Thévenin impedance seen at the inverter's terminals is high. However, existing (conventional) current regulator designs for such inductive-capacitive-inductive (*LCL*)-filtered inverters do not account for significant grid impedance variations. This paper proposes an optimized current regulator design for proportional-integral (PI) and P+resonant (PR) controller classes of *LCL*-filtered grid-feeding inverters operating under weak grid conditions. We show that two crucial crossover frequencies must be used in the design process to maximize the current regulator's proportional gain and minimize its integrator reset time. We experimentally validate the design using a three-phase grid-feeding inverter, demonstrating improved performance over a conventional design approach.**

***Index Terms*—Current regulation, grid-connected inverter, proportional-integral (PI), P+resonant (PR), weak grid.**

I. Introduction

Inverters are increasingly becoming the backbone of modern power grids, driven by a paradigm shift towards renewable energy-based electricity generation catalyzed by global warming concerns. Grid-feeding inverters (also known as grid-following) are now ubiquitous, operating as current sources synchronized to the grid voltage waveform through phase-locked loops (PLLs). While *LCL* filters are used to interface such inverters to the grid owing to their excellent harmonic attenuation, the filter's resonance can introduce stability challenges [1]. Weak grid conditions characterized by high impedance, which can occur when remotely located generators connect to the grid using long transmission lines or to power grid areas with sparse transmission infrastructure, can exacerbate these issues as the filter's resonant frequency shifts as a function of the grid impedance [2]. The inverter controls are also susceptible to instability under such conditions [3].

Virtual impedance shaping is a method used to improve stability under grid impedance variations by augmenting the inverter's output impedance, and thus its interaction with the grid [4]. Moreover, active damping is another stability-enhancing method, which feeds control measurements back as damping terms, emulating a virtual resistor [5]. While capacitor current feedback is a popular damping method, the computation and modulation delays inherent in digital control systems have a destabilizing effect, particularly as the *LCL* filter resonant frequency approaches one-sixth of the sampling frequency, which induces design constraints and stability limits in practice [6]. Hence, Pan *et al.* proposed a capacitor-current-feedback active damping scheme with reduced computation delay [2]. Other active damping schemes have also been proposed, including grid-current feedback [7], [8], capacitor current feedback with a phase-lead compensator [9], and inverter-current feedback with high-frequency phase compensation [10]. Additionally, feedforward [1] and passivity-based methods have been used to address weak grid stability challenges [11].

The PLL is another potential source of inverter instability owing to the quadrature-axis impedance behaving as a negative resistor [12]. Limiting the PLL's bandwidth reduces the range of negative resistance, which can help with inverter stability at the expense of dynamic performance. Impedance-shaping [13] and redesigning the PLL [14] and current regulator [15] parameters are other methods proposed to overcome this effect. However, these methods could degrade transient and fault-ride-through performance.

While analytical PI and PR current regulator designs for L-filtered inverters have been proposed for weak grid conditions, e.g., [16], a gap exists for *LCL*-filtered variants. For example, Parker *et al.* [17] demonstrated the applicability of design concepts presented in [18] to inverters employing grid-current feedback active damping and an *LCL* filter with a high resonant frequency. However, large grid impedance variations were not considered. Moreover, although the design of a current regulator's proportional gain was presented in [19] for an *LCL*-filtered inverter through a power quality lens, open questions remain regarding how to design both the proportional gain and integrator reset time in the weak grid context. Hence, this paper proposes an analytical framework to bridge this gap, which we validate experimentally to showcase the performance improvement over a conventional design approach.

II. Inverter Dynamic Laplace Domain Model

This work considers *LCL*-filtered grid-feeding inverters like the general topology shown in Fig. 1, where L_1 represents the inverter-side inductance, C_f is the filter capacitance, and L_2 is the grid-side inductance, respectively. We represent the grid connection using a Thévenin impedance in series with an ideal voltage source, where L_g and R_g denote the grid inductance and resistance, respectively. The inverter synchronizes to the grid voltage waveform via a phase-locked loop (PLL), and

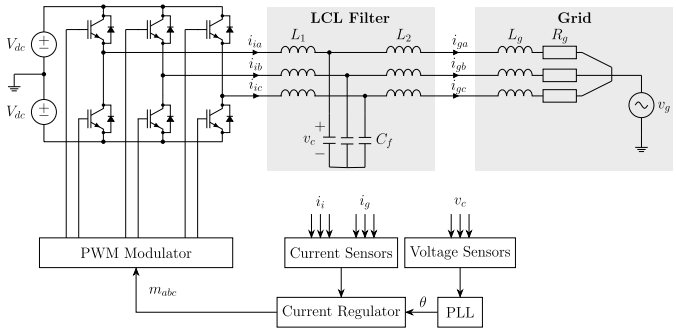


Fig. 1. *LCL*-filtered grid-connected VSI with a general current control strategy.

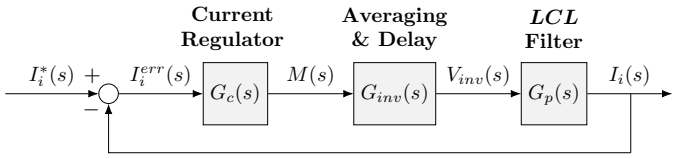


Fig. 2. Block diagram representation comprising current regulator, inverter averaging, PWM sampling and transport delays, and an *LCL* filter.

we can employ PI or PR control for the overarching current regulation strategy. Fig. 2 shows the block diagram representation of the inverter's averaged closed-loop current regulation process, including the current regulator, PWM transport and sampling delay, and *LCL* filter. We define the transfer functions for the PI or PR controller in the s-domain by

$$G_{PI}(s) = K_p\left(1 + \frac{1}{s\tau_r}\right) = \frac{K_p}{\tau_r}\left(\frac{s\tau_r + 1}{s}\right) \tag{1}$$

$$G_{PR}(s) = K_p\left(1 + \frac{1}{\tau_r}\frac{s}{s^2 + {\omega_0}^2}\right) = \frac{K_p}{\tau_r}\left(\frac{s^2\tau_r + s + {\omega_0}^2\tau_r}{s^2 + {\omega_0}^2}\right) \tag{2}$$

where K_p corresponds to the current regulator's proportional gain, τ_r is the integrator reset time, and ω_0 is the resonator target reference angular frequency, respectively. However, at high frequencies, both transfer functions converge to K_p, viz., $G_{PI}(j\omega) \to K_p$ and $G_{PR}(j\omega) \to K_p$ as $\omega \to \infty$. As such, the PI controller is sufficient for initial frequency domain synthesis, and we consider $G_c(s) = G_{PI}(s)$.

Moreover, we model the voltage-source inverter (VSI) as a linear gain with transport delay according to

$$G_{inv}(s) = V_{dc}e^{-sT_d} \tag{3}$$

where V_{dc} is one-half the total DC link voltage and T_d is the time delay associated with the PWM transport and sampling. For the plant characteristics, we first describe the total equivalent impedance between the grid and the VSI by

$$Z_{eq}(s) = \frac{s^3C_fL_{\sum}L_1 + sL_t}{s^2C_fL_{\sum} + 1} \tag{4}$$

where $L_{\sum} = L_2 + L_g$ and $L_t = L_1 + L_{\sum}$. Hence, the *LCL* admittance is the reciprocal of (4), viz.

$$\begin{aligned} Y_{eq}(s) &= \frac{1}{Z_{eq}(s)} = \frac{s^2C_fL_{\sum} + 1}{s^3C_fL_{\sum}L_1 + sL_t} \\ &= \frac{s^2C_fL_{\sum} + 1}{sL_t\left[\frac{s^2C_fL_{\sum}L_1}{L_t} + 1\right]} = \frac{1}{sL_t}\frac{\left(\frac{s}{\omega_{ar}}\right)^2 + 1}{\left(\frac{s}{\omega_{res}}\right)^2 + 1} \end{aligned} \tag{5}$$

where ω_{ar} and ω_{res} correspond to the *LCL* filter's anti-resonant and resonant angular frequency, respectively. This admittance transfer function has a first-order inductive characteristic, followed by anti-resonant and resonant notches. The anti-resonant and resonant frequencies are governed by the *LCL* filter parameters, viz.

$$\omega_{ar} = \frac{1}{\sqrt{C_fL_{\sum}}} = \frac{1}{\sqrt{C_f(L_2 + L_g)}} \tag{6}$$

$$\omega_{res} = \frac{1}{\sqrt{\frac{C_fL_{\sum}L_1}{L_t}}} = \frac{1}{\sqrt{\frac{C_f(L_2+L_g)L_1}{L_1+L_2+L_g}}}. \tag{7}$$

Therefore, the admittance's phase characteristic satisfies

$$\angle Y_{eq}(j\omega) = \begin{cases} -\frac{\pi}{2}, & \omega < \omega_{ar} \\ +\frac{\pi}{2}, & \omega_{ar} \le \omega \le \omega_{res} \\ -\frac{\pi}{2}, & \omega > \omega_{res}, \end{cases} \tag{8}$$

and its magnitude characteristic is given by

$$\left|Y_{eq}(j\omega)\right| = \frac{1}{\omega L_t}\frac{\left|1 - \left(\frac{\omega}{\omega_{ar}}\right)^2\right|}{\left|1 - \left(\frac{\omega}{\omega_{res}}\right)^2\right|}. \tag{9}$$

The asymptotic behavior of the magnitude response is thus

$$\left|Y_{eq}(j\omega)\right| \to \begin{cases} \frac{1}{\omega L_t}, & \omega \ll \omega_{ar} \\ \frac{1}{\omega L_t}\left(\frac{\omega_{res}}{\omega_{ar}}\right)^2 = \frac{1}{\omega L_t}\left(1 + \frac{L_{\sum}}{L_1}\right), & \omega \gg \omega_{res}. \end{cases} \tag{10}$$

That is, the admittance curve is asymptotically enhanced by $\left(1 + \frac{L_{\sum}}{L_1}\right)$ at high frequencies.

Using (1), (3) and (5), we define the current regulator's overall forward path gain (FPG) as

$$\begin{aligned} FPG_{LCL}(s) &:= G_{PI}(s) \cdot G_{VSI}(s) \cdot Y_{eq}(s) \\ &= \frac{K_p}{\tau_r}\left(\frac{s\tau_r + 1}{s}\right) \cdot V_{dc}e^{-sT_d} \cdot \frac{1}{sL_t}\frac{\left(\frac{s}{\omega_{ar}}\right)^2 + 1}{\left(\frac{s}{\omega_{res}}\right)^2 + 1}. \end{aligned} \tag{11}$$

However, if we neglect the effects of the high *LCL* resonance and anti-resonance terms, we can approximate (11) by

$$\begin{aligned} FPG_{L_t}(s) &= G_{PI}(s) \cdot G_{VSI}(s) \cdot \frac{1}{sL_t} \\ &= \frac{K_p}{\tau_r}\left(\frac{s\tau_r + 1}{s}\right) \cdot V_{dc}e^{-sT_d} \cdot \frac{1}{sL_t}. \end{aligned} \tag{12}$$

III. First-order Inductive Filter Synthesis

We briefly consider the first-order inductive plant characteristic, where the frequency response of the controller FPG presented in (12) is given by

$$\angle FPG_{L_t}(j\omega) = -\pi + \tan^{-1}(\omega\tau_r) - \omega T_d \tag{13}$$

$$\left|FPG_{L_t}(j\omega)\right| = \frac{V_{dc}K_p}{\omega^2\tau_r L_t}\sqrt{(\omega\tau_r)^2+1}. \tag{14}$$

Applying the Nyquist stability criterion at the unity gain crossover frequency $\omega_{c(L)}$ requires that

$$\angle FPG_{L_t}\left(j\omega_{c(L)}\right) = -\pi + \tan^{-1}\left(\omega_{c(L)}\tau_r\right) - \omega_{c(L)}T_d = -\pi + \phi_m \tag{15}$$

$$\left|FPG_{L_t}\left(j\omega_{c(L)}\right)\right| = \frac{V_{dc}K_p}{{\omega_{c(L)}}^2\tau_r L_t}\sqrt{\left(\omega_{c(L)}\tau_r\right)^2+1} = 1. \tag{16}$$

Assuming that $\omega_{c(L)}\tau_r \gg 1$, we can simplify (15) to

$$\angle FPG_{L_t}\left(j\omega_{c(L)}\right) = -\pi + \frac{\pi}{2} - \omega_{c(L)}T_d = -\pi + \phi_m, \tag{17}$$

then, rearrange for the crossover frequency, viz.

$$\omega_{c(L)} = \frac{\frac{\pi}{2} - \phi_m}{T_d}. \tag{18}$$

Moreover, the magnitude response at the unity gain is

$$\left|FPG_{L_t}\left(j\omega_{c(L)}\right)\right| = \frac{V_{dc}K_p}{\omega_{c(L)}L_t} = 1, \tag{19}$$

which we can rearrange for the proportional gain, yielding

$$K_p = \frac{\omega_{c(L)}L_t}{V_{dc}}. \tag{20}$$

These are the classic relationships for an inductive filter, showing that we must use the entire series inductance combination (including the grid inductance) when determining K_p (refer to [16] for the complete synthesis of an L-filtered inverter operating in a weak grid context).

IV. Third-order *LCL* filter synthesis

We now consider the frequency response of the controller FPG with the third-order *LCL* plant characteristic given by (11), viz.

$$\angle FPG_{LCL}(j\omega) = \begin{cases} -\pi + \tan^{-1}(\omega\tau_r) - \omega T_d, & \omega < \omega_{ar} \\ \tan^{-1}(\omega\tau_r) - \omega T_d, & \omega_{ar} \le \omega \le \omega_{res} \\ -\pi + \tan^{-1}(\omega\tau_r) - \omega T_d, & \omega > \omega_{res} \end{cases} \tag{21}$$

$$\left|FPG_{LCL}(j\omega)\right| = \frac{V_{dc}K_p}{\omega^2\tau_r L_t}\sqrt{(\omega\tau_r)^2+1}\frac{\left|1-\left(\frac{\omega}{\omega_{ar}}\right)^2\right|}{\left|1-\left(\frac{\omega}{\omega_{res}}\right)^2\right|}. \tag{22}$$

This response contains several salient features. First, the phase follows the conventional response of an inductive filter outside the anti-resonant and resonant frequencies, i.e., $\forall\omega \in \{\omega : \omega < \omega_{ar} \text{ or } \omega > \omega_{res}\}$. Moreover, there is an additional 180° phase enhancement within these frequencies. Combined with the high gain enhancement owing to the resonance, the unity gain crossover frequency must be above the resonance. Hence, there are limits on the allowable resonant frequency to ensure stability. We can determine the critical resonant frequency from the high frequency phase response by considering the Nyquist threshold, viz.

$$\angle FPG_{LCL}(j\omega_{crit}) = -\pi + \tan^{-1}(\omega_{crit}\tau_r) - \omega_{crit}T_d = -\pi \tag{23}$$

where ω_{crit} is the critical resonant frequency. Hence,

$$\omega_{crit} = \frac{\pi}{2T_d} = \frac{\pi}{3T} = \frac{2\pi}{3}f_c \tag{24}$$

where f_c is the carrier frequency for an asymmetric regular sampled pulse width modulator (i.e., double update mode). This means that ω_{res} must be less than ω_{crit} to enable a stable response, and the high frequency *LCL* crossover must occur after ω_{res}. Within this constraint, we identify several distinct cases requiring independent treatment, viz.

1) When the resonance is **below** the first-order nominal crossover frequency, i.e., $\omega_{res} < \omega_{c(L)}$.
2) When the resonance is **above** the first-order nominal crossover frequency, i.e., $\omega_{res} > \omega_{c(L)}$.

A. Case I: Resonance below the first-order nominal crossover frequency

When the *LCL* filter's resonance is below the first-order nominal crossover frequency, the FPG's phase profile at high frequency converges to

$$\angle FPG_{LCL}\left(j\omega_{c(LCL)}\right) = -\pi + \tan^{-1}\left(\omega_{c(LCL)}\tau_r\right) - \omega_{c(LCL)}T_d. \tag{25}$$

Applying the Nyquist stability criterion produces the same result as for the first-order inductive filter under the same assumption that $\omega_{c(LCL)}\tau_r \gg 1$, viz.

$$\angle FPG_{LCL}\left(j\omega_{c(LCL)}\right) = -\pi + \tan^{-1}\left(\omega_{c(LCL)}\tau_r\right) - \omega_{c(LCL)}T_d = -\pi + \phi_m \tag{26}$$

which we can rearrange to

$$\omega_{c(LCL)} = \frac{\frac{\pi}{2} - \phi_m}{T_d}. \tag{27}$$

The magnitude response at this frequency gives

$$\left|FPG_{LCL}\left(j\omega_{c(LCL)}\right)\right| = \frac{V_{dc}\,K_p\,\xi}{{\omega_{c(LCL)}}^2\tau_r L_t}\frac{\left|1-\left(\frac{\omega_{c(LCL)}}{\omega_{ar}}\right)^2\right|}{\left|1-\left(\frac{\omega_{c(LCL)}}{\omega_{res}}\right)^2\right|} = 1. \tag{28}$$

where $\xi = \sqrt{\left(\omega_{c(LCL)}\tau_r\right)^2+1}$. By again considering that $\omega_{c(LCL)}\tau_r \gg 1$, we simplify (28) to

$$\left|FPG_{LCL}\left(j\omega_{c(LCL)}\right)\right| = \frac{V_{dc}K_p}{\omega_{c(LCL)}L_t}\frac{\left|1-\left(\frac{\omega_{c(LCL)}}{\omega_{ar}}\right)^2\right|}{\left|1-\left(\frac{\omega_{c(LCL)}}{\omega_{res}}\right)^2\right|} = 1. \tag{29}$$

Rearranging (29) for the proportional gain K_p leads to

$$K_p = \frac{\omega_{c(LCL)} L_t}{V_{dc}} \frac{\left|1 - \left(\frac{\omega_{c(LCL)}}{\omega_{res}}\right)^2\right|}{\left|1 - \left(\frac{\omega_{c(LCL)}}{\omega_{ar}}\right)^2\right|} = \frac{\omega_{c(LCL)}}{V_{dc}} \frac{\left|L_t - {\omega_{c(LCL)}}^2 C_f L_\sum L_1\right|}{\left|1 - {\omega_{c(LCL)}}^2 C_f L_\sum\right|}. \quad (30)$$

If the resonant frequency is sufficiently small compared to the *LCL* crossover frequency (i.e., $\omega_{res} < 0.3\,\omega_{c(LCL)}$) it is possible to apply the asymptotic limit approximations, leading to

$$K_p = \frac{\omega_{c(LCL)} L_t}{V_{dc}} \frac{{\omega_{ar}}^2}{{\omega_{res}}^2} = \frac{\omega_{c(LCL)} L_1}{V_{dc}}. \quad (31)$$

That is, the proportional gain is selected on the basis of the inverter-side inductance only.

B. Case II: Resonance above the first-order nominal crossover frequency

In this case, the first-order nominal crossover frequency falls within the range $\omega_{ar} \leq \omega_{c(L)} \leq \omega_{res}$. However, due to the high gain of the *LCL* resonance this nominal crossover frequency cannot be realized, and the actual crossover frequency must occur above the resonant frequency. It is therefore necessary to assess the upper bound on the highest achievable phase margin by quantifying the forward path phase response just beyond the resonance, viz.

$$\angle FPG_{LCL}\left(j\omega_{res}\right) = -\frac{\pi}{2} - \omega_{res} T_d. \quad (32)$$

Hence,

$$\phi_{m_{ub}} = \frac{\pi}{2} - \omega_{res} T_d. \quad (33)$$

If this bound is sufficiently large it may be possible to design the current regulator to achieve a similar phase margin by selecting an actual crossover frequency above the resonance with a small margin (e.g., 10%), and to then use the FPG response to set the proportional gain, i.e.,

$$\omega_{c(LCL)} = 1.1 \times \omega_{res}, \quad \phi_{m(LCL)} = \frac{\pi}{2} - \omega_{c(LCL)} T_d$$

$$K_p = \frac{\omega_{c(LCL)} L_t}{V_{dc}} \frac{\left|1 - \left(\frac{\omega_{c(LCL)}}{\omega_{res}}\right)^2\right|}{\left|1 - \left(\frac{\omega_{c(LCL)}}{\omega_{ar}}\right)^2\right|} = \frac{\omega_{c(LCL)}}{V_{dc}} \frac{\left|L_t - {\omega_{c(LCL)}}^2 C_f L_\sum L_1\right|}{\left|1 - {\omega_{c(LCL)}}^2 C_f L_\sum\right|}. \quad (34)$$

Note that it will not be possible (in general) to use asymptotic approximations for the *LCL* resonance terms.

C. Reset time synthesis

As the grid inductance increases, the resonant and anti-resonant frequencies reduce and diverge from one another, viz.

$$\omega_{ar} = \frac{1}{\sqrt{C_f\left(L_2 + L_g\right)}} \quad \text{(decreases with } L_g\text{)} \quad (35)$$

$$\omega_{res} = \frac{1}{\sqrt{\frac{C_f(L_2+L_g)L_1}{L_1+L_2+L_g}}} \quad \text{(decreases with } L_g\text{)} \quad (36)$$

$$\frac{\omega_{res}}{\omega_{ar}} = \sqrt{1 + \frac{L_2 + L_g}{L_1}} \quad \text{(increases with } L_g\text{)}. \quad (37)$$

Hence, the lower crossover frequency $\omega_{c(min)}$ from the *LCL* anti-resonance notch can also impact the phase margin. This frequency can be found from the magnitude response, viz.

$$\left|FPG_{LCL}\left(j\omega_{c(min)}\right)\right| = \frac{K_p V_{dc}\,\eta}{{\omega_{c(min)}}^2 L_t \tau_r} \frac{1 - \left(\frac{\omega_{c(min)}}{\omega_{ar}}\right)^2}{1 - \left(\frac{\omega_{c(min)}}{\omega_{res}}\right)^2} = 1. \quad (38)$$

where $\eta = \sqrt{\left(\omega_{c(min)}\tau_r\right)^2 + 1}$.

Assuming that $\omega_{c(min)}$ is well below both ω_{ar} and ω_{res}, then the asymptotic approximation for the *LCL* filter can be applied, leading to

$$\left|FPG_{LCL}\left(j\omega_{c(min)}\right)\right| = \frac{K_p V_{dc}\sqrt{\left(\omega_{c(min)}\tau_r\right)^2 + 1}}{{\omega_{c(min)}}^2 L_t \tau_r} = 1. \quad (39)$$

Simultaneously, for frequencies below the anti-resonance, the FPG phase response should satisfy

$$\angle FPG_{LCL}\left(j\omega_{c(min)}\right) = -\pi + \tan^{-1}\left(\omega_{c(min)}\tau_r\right) - \omega_{c(min)} T_d. \quad (40)$$

Recognizing that the $\omega_{c(min)} T_d$ phase contribution will typically be small at these frequencies, then applying the Nyquist stability criterion requires that

$$\tan^{-1}\left(\omega_{c(min)}\tau_r\right) = \phi_m \implies \omega_{c(min)}\tau_r = \tan\left(\phi_m\right). \quad (41)$$

Hence,

$$\omega_{c(min)} = \frac{K_p V_{dc}\sqrt{\tan^2\left(\phi_m\right) + 1}}{L_t \tan\left(\phi_m\right)} = \frac{K_p V_{dc}}{L_t \sin\left(\phi_m\right)}. \quad (42)$$

Substituting K_p from (34) into (42) yields

$$\omega_{c(min)} = \frac{\omega_{c(LCL)}}{L_t \sin\left(\phi_m\right)} \frac{\left|L_t - {\omega_{c(LCL)}}^2 C_f L_\sum L_1\right|}{\left|1 - {\omega_{c(LCL)}}^2 C_f L_\sum\right|}. \quad (43)$$

Consequently, the integrator reset time is, viz.

$$\tau_r = \frac{\tan\left(\phi_m\right)}{\omega_{c(min)}} = \frac{\sin^2\left(\phi_m\right) L_t \left|1 - {\omega_{c(LCL)}}^2 C_f L_\sum\right|}{\cos\left(\phi_m\right)\omega_{c(LCL)}\left|L_t - {\omega_{c(LCL)}}^2 C_f L_\sum L_1\right|}. \quad (44)$$

When implementing a PR control scheme, this solution can only be possible if $\omega_{c(min)}$ is larger than the target fundamental frequency, otherwise the fundamental frequency resonator

will interact with the desired low frequency crossover. This will typically require that $\omega_{c(min)}$ is at least 30% larger than the fundamental frequency to ensure that the low frequency crossover occurs in the asymptotic region of the fundamental frequency resonator. If this is not the case, then it will be necessary to constrain $\omega_{c(min)}$, and assess whether the achievable low frequency phase margin is acceptable.

In such situations, we define the low crossover frequency as $\omega_{c(min)} = 1.3\omega_0$. Then, rearranging (39) yields

$$\tau_r = \frac{1}{\omega_{c(min)}\sqrt{\left(\frac{\omega_{c(min)}L_t}{K_p V_{dc}}\right)^2 - 1}}. \tag{45}$$

This is likely to result in a very small phase margin in practice since, from the FPG transfer function, the actual phase margin at the minimum crossover frequency will be $\phi_{m(min)} = \tan\left(\omega_{c(min)}\tau_r\right)$, viz.

$$\phi_{m(min)} = \tan\left(\frac{1}{\sqrt{\left(\frac{\omega_{c(min)}L_t}{K_p V_{dc}}\right)^2 - 1}}\right). \tag{46}$$

If $\omega_{c(min)}L_t \gg K_p V_{dc}$, then this will be an inadequate phase margin.

However, this is not likely to be realistic, and it would be necessary to consider the effects of the fundamental frequency resonator, which will introduce significant gain in this vicinity. If we include this effect, the FPG transfer function with a PR controller is given by:

$$FPG_{LCL}(s) = \frac{K_p}{\tau_r}\left[\frac{\tau_r s^2 + s + \tau_r {\omega_0}^2}{s^2 + {\omega_0}^2}\right] \cdot V_{dc}e^{-sT_d} \cdot \frac{1}{sL_t}\frac{\left(\frac{s}{\omega_{ar}}\right)^2 + 1}{\left(\frac{s}{\omega_{res}}\right)^2 + 1}. \tag{47}$$

At the lower crossover frequency, applying the asymptotic approximation for the *LCL* filter gives

$$FPG_{LCL}\left(j\omega_{c(min)}\right) = \frac{K_p}{\tau_r}\left[\frac{\tau_r\left({\omega_0}^2 - {\omega_{c(min)}}^2\right) + j\omega_{c(min)}}{{\omega_0}^2 - {\omega_{c(min)}}^2}\right]\gamma \tag{48}$$

where

$$\gamma = \frac{V_{dc}e^{-j\omega_{c(min)}T_d}}{j\omega_{c(min)}L_t}. \tag{49}$$

Hence, the FPG magnitude and phase response are as follows

$$\left|FPG_{LCL}\left(j\omega_{c(min)}\right)\right| = \frac{K_p V_{dc}}{\omega_{c(min)}L_t\tau_r}\frac{\alpha}{\left|{\omega_0}^2 - {\omega_{c(min)}}^2\right|} \tag{50}$$

$$\angle FPG_{LCL}\left(j\omega_{c(min)}\right) = \begin{cases} -\frac{\pi}{2} + \tan^{-1}(\beta) - \omega_{c(min)}T_d & \text{(51a)} \\ -\frac{\pi}{2} - \tan^{-1}(\beta) - \omega_{c(min)}T_d, & \text{(51b)} \end{cases}$$

where

$$\alpha = \sqrt{{\omega_{c(min)}}^2 + {\tau_r}^2\left({\omega_0}^2 - {\omega_{c(min)}}^2\right)^2}, \tag{52}$$

and

$$\beta = \frac{\omega_{c(min)}}{\tau_r\left({\omega_0}^2 - {\omega_{c(min)}}^2\right)}, \tag{53}$$

and where (51a) and (51b) correspond to cases where $\omega_{c(min)} < \omega_0$ and $\omega_{c(min)} > \omega_0$, respectively.

Using $\omega_{c(min)} = 1.3\omega_0$, the reset time can be found by applying the Nyquist criterion, viz.

$$-\frac{\pi}{2} - \tan^{-1}\left(\frac{\omega_{c(min)}}{\tau_r\left({\omega_{c(min)}}^2 - {\omega_0}^2\right)}\right) \approx -\pi + \phi_m. \tag{54}$$

Hence,

$$\tau_r = \frac{\omega_{c(min)}}{\left({\omega_{c(min)}}^2 - {\omega_0}^2\right)\tan\left(\frac{\pi}{2} - \phi_m\right)}. \tag{55}$$

Moreover, from (50)

$$K_p = \frac{\omega_{c(min)}L_t}{V_{dc}}\frac{\left({\omega_{c(min)}}^2 - {\omega_0}^2\right)\tau_r}{\sqrt{{\omega_{c(min)}}^2 + {\tau_r}^2\left({\omega_{c(min)}}^2 - {\omega_0}^2\right)^2}} = \frac{\omega_{c(min)}L_t}{V_{dc}}\frac{1}{\sqrt{\tan^2\left(\frac{\pi}{2} - \phi_m\right) + 1}}. \tag{56}$$

V. Current Regulator Forward Path Gain Frequency Response

To validate the *LCL*-filtered current regulator gain synthesis concepts established in Sections III and IV, we develop Bode plots of the current regulator FPG transfer functions using MATLAB, based on the parameters given in Table I. We consider two different capacitor values, allowing for low and high resonant frequencies relative to the first-order nominal crossover frequency $\omega_{c(L)}$. Moreover, we select a nominal controller phase margin of 60° to provide closed-loop damping associated with a 5% overshoot for current reference step changes [20].

Fig. 3 compares the PI and PR current regulator behavior considering both *L* and *LCL* asymptotic characteristics using the K_p parameters defined in (20) and (31) when ω_{res} is below the nominal first-order crossover frequency $\omega_{c(L)}$. The first-order characteristics (in black) show the well-established high frequency convergence of the PI and PR current regulators, achieving the desired cross-over frequency $\omega_{c(L)}$ and phase margin ϕ_m when the gain formulation considers the totality of the series inductance. However, the high frequency gain

TABLE I
System Parameters.

Parameter	Value	Parameter	Value
$2V_{dc}$	400 V	L_1	5 mH
f_{sw}	10 kHz	L_2	4.2 mH
f_{grid}	50 Hz	v_{grid}	207 V_{rms}
T_{sample}	50 µs	ω_{crit}	20.9 krad s^{-1}
ϕ_m	60°	$\omega_{c(L)}$	6.98 krad s^{-1}
$C_{f(lo)}$	15 µF	$\omega_{res(lo)}$	5.4 krad s^{-1}
$C_{f(hi)}$	4.7 µF	$\omega_{res(hi)}$	9.65 krad s^{-1}
S_{base}	5000 VA	V_{base}	220 V_{rms}
L_{base}	30.8 mH	Z_{base}	9.68 Ω

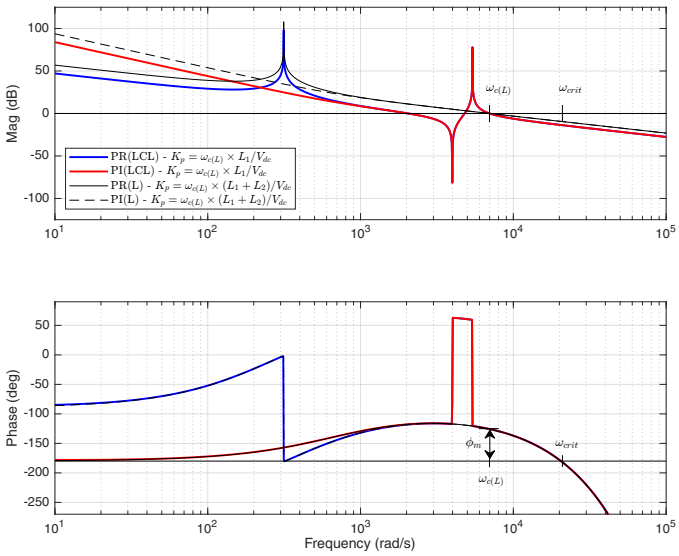


Fig. 3. Frequency response of the current regulator forward path gain considering LCL resonance below the 1^{st} order crossover frequency.

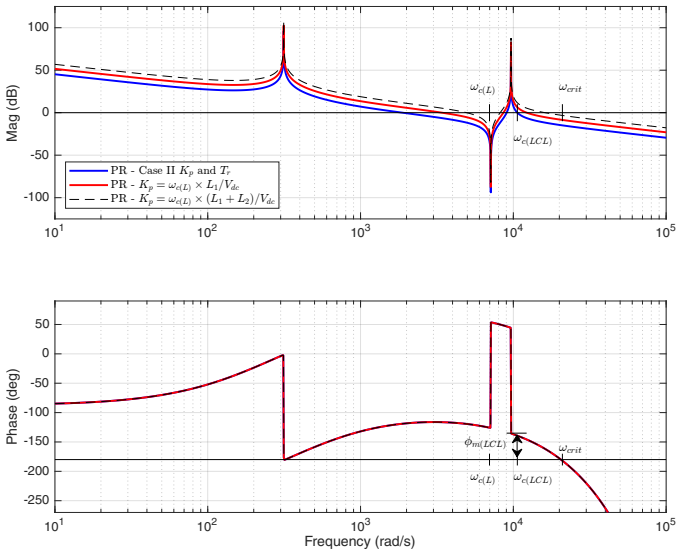


Fig. 4. Frequency response of the current regulator forward path gain considering LCL resonance above the 1^{st} order crossover frequency.

enhancement associated with the *LCL* filter means that a reduced proportional gain based on just the inverter side inductance L_1 is needed to achieve the same controller gain margins when the true third-order *LCL* plant characteristic is accounted for.

Fig. 4 shows the scenario when the *LCL* resonance is above the nominal first-order crossover frequency $\omega_{c(L)}$. This confirms that it is not possible to achieve the desired phase margin ϕ_m, since it is necessary for stability to crossover above ω_{res}. If the proportional gain K_p is based on the inverter-side inductance, or even the totality of the *ac* side inductance, the result is a crossover frequency well above the intended $\omega_{c(L)}$ and a significantly degraded phase margin. However, when the gain parameter based on (34) is applied

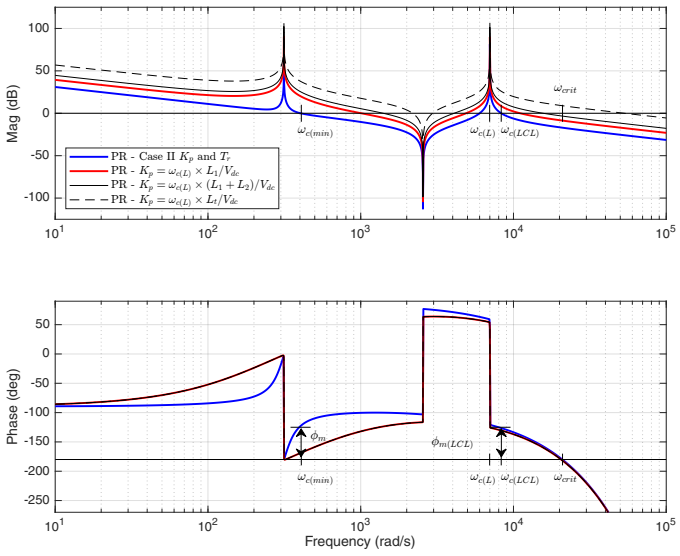


Fig. 5. Frequency response of the current regulator forward path gain accounting for the impact of a weak grid - $L_g = 28.4$ mH $= 0.92$ p.u.

while forcing a crossover frequency $\omega_{c(LCL)}$ just 10% above ω_{res}, a stable current regulator results with a phase margin $\phi_{m(LCL)}$ that is in the vicinity of the original target ϕ_m.

Fig. 5 illustrates the scenario when the grid is weakened, with a 0.92 p.u. series inductance. The separation of the *LCL* resonant peak and anti-resonant notch is clearly apparent. Closed-loop instability results if the totality of the *ac* side inductance is considered in the formulation of K_p. In contrast, stable responses occur when K_p is synthesized based on either just $L_1 + L_2$ or L_1, albeit with crossover frequencies well above the actual ω_{res} with significantly degraded phase margins. To address this, the gain synthesis concepts of Section IV have been applied to enforce a high frequency crossover $\omega_{c(LCL)}$ much closer to the actual *LCL* ω_{res}. However, this consequently reduces the forward path gain in the vicinity of the PR resonant frequency ω_o, which would degrade the phase margin associated with the low-frequency crossover $\omega_{c(min)}$. This is managed by enforcing the low-frequency crossover to occur just above ω_o (i.e., 30%), and setting the reset time based on (55). The result is a current regulator with both acceptable high and low frequency stability margins.

VI. Experimental Validation

The analytical current regulator synthesis framework has been validated experimentally using a VSI with the high *LCL* resonant frequency parameters detailed in Table I (i.e., utilizing $C_{f(hi)}$), and using the self-synchronising stationary frame current regulation scheme shown in Fig. 6. Current regulation is achieved via a pair of PR controllers which operate on the phase a and b inverter currents, with the third phase-leg modulated based on the negative sum of the a and b PWM command signals [21]. A synchronous reference frame PLL (SRF-PLL) estimates the grid voltage phase angle using the second-order generalized integrator (SOGI) outputs to generate the sinusoidal current references. Meanwhile, the PLL's

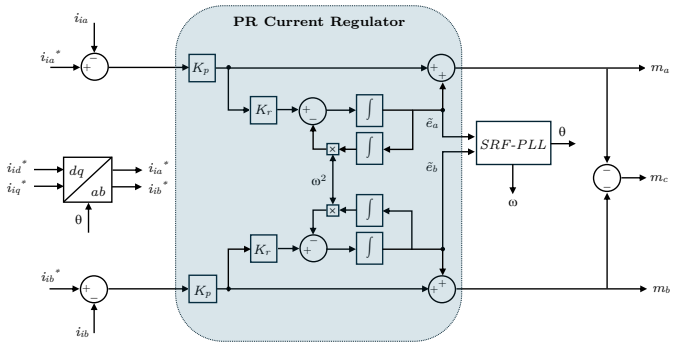


Fig. 6. Self-synchronizing inverter current feedback scheme.

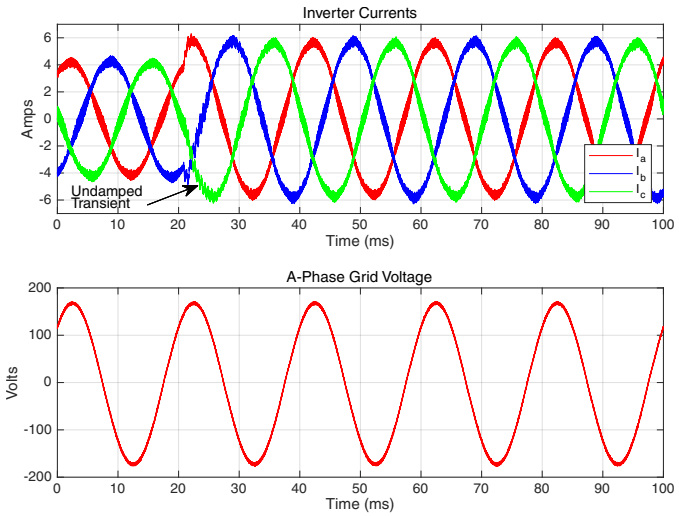


Fig. 7. Experimental current regulator response with the proportional gain based on (31), and with $L_g = 0$ mH.

estimated frequency is fed back into the SOGI resonators, tuning its resonant frequency. The self-synchronizing control algorithms were implemented using a TMS320F2812 fixed-point processor controller board, directly controlling a three-phase current-regulated VSI. A California Instruments MX30 grid emulator was used to establish the grid conditions, with a series inductance added to weaken the grid connection.

Fig. 7 shows the inverter's experimental response with $L_g = 0$ mH (i.e., 0 p.u. and the total grid-side inductance only comprises L_2) using the conventional current regulator gains based on (31). The target current reference steps from 4 A to 6 A at $t = 20$ ms and the controller's response is swift, tracking the current reference, albeit with a noticeable level of high frequency ringing in phases b and c lasting for approximately one-quarter of a fundamental cycle. In contrast, Fig. 8 shows the experimental response with $L_g = 0$ mH using the current regulator proportional gain based on (34). The response shows a similar transient capability, but with a noticeably reduced level of high frequency oscillation following the change in current reference.

Fig. 9 shows the current regulator behavior for the weak grid scenario (i.e., $L_g = 28.4$ mH = 0.92 p.u.) based on the

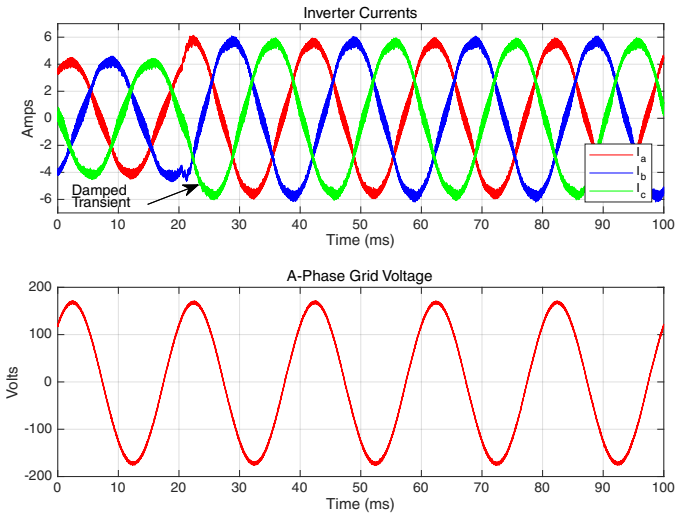


Fig. 8. Experimental response with the proportional gain based on (34), and with $L_g = 0$ mH.

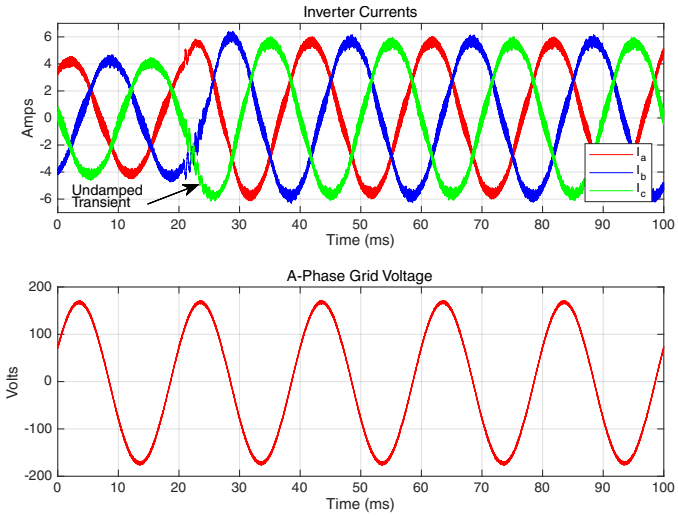


Fig. 9. Experimental current regulator response with the proportional gain based on (31), and with $L_g = 28.4$ mH = 0.92 p.u.

conventional current regulator proportional gain using (31). Again, a high frequency undamped oscillation is evident after the transient change in the current reference, and there is also a degree of low frequency overshoot apparent in phase b. In contrast, Fig. 10 shows the experimental response when the proportional gain and reset time are set to match the blue characteristic of Fig. 5. In this case, the transient step change is associated with a damped high frequency oscillatory response. The resonator settling time has increased as a consequence of the larger τ_r value, but this is a necessary trade-off to ensure current regulator stability in a weak grid context.

VII. Conclusion

This paper presents an analytical approach for designing PI and PR current regulators for *LCL*-filtered grid-feeding inverters operating under weak grid conditions. We show that

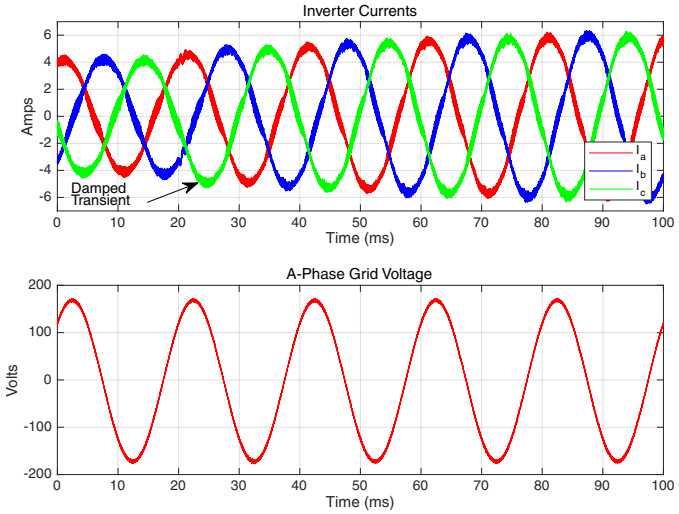


Fig. 10. Experimental current regulator response with the proportional gain based on (56) and reset time based on (55), and with $L_g = 28.4$ mH = 0.92 p.u.

the minimum and maximum crossover frequencies are imperative to the design process to maximize the current regulator's proportional gain and minimize its integrator reset time. As the grid inductance increases, the frequency range between the resonant and anti-resonant peaks progressively increases, and a gain lift occurs in the high-frequency region. Hence, the minimum crossover frequency can vary significantly as a function of the grid inductance. As such, two key design cases exist depending on whether the *LCL* filter's resonance is below or above the first-order nominal frequency. In the former situation, we can select the proportional gain on the basis of only the inverter-side inductance. In contrast, if the nominal frequency falls between the *LCL* resonance and anti-resonance, we propose selecting a crossover frequency just beyond ω_{res}, and designing the proportional gain accordingly. Moreover, the integrator reset time is selected by accounting for the minimum crossover frequency, where the phase margin can be affected by the *LCL* filter's anti-resonance. Experimental results demonstrate that the proposed design methodology produces stable, well-damped responses under high grid inductance values for a three-phase grid-feeding VSI, in contrast to conventional gains that yielded significant ringing given a step change in the target current reference.

REFERENCES

[1] X. Li, J. Fang, Y. Tang, X. Wu, and Y. Geng, "Capacitor-voltage feedforward with full delay compensation to improve weak grids adaptability of LCL-filtered grid-connected converters for distributed generation systems," *IEEE Trans. Power Electron.*, vol. 33, no. 1, pp. 749–764, 2018.

[2] D. Pan, X. Ruan, C. Bao, W. Li, and X. Wang, "Capacitor-current-feedback active damping with reduced computation delay for improving robustness of LCL-type grid-connected inverter," *IEEE Trans. Power Electron.*, vol. 29, no. 7, pp. 3414–3427, 2014.

[3] X. Fu, J. Sun, M. Huang, Z. Tian, H. Yan, H. H.-C. Iu, P. Hu, and X. Zha, "Large-signal stability of grid-forming and grid-following controls in voltage source converter: A comparative study," *IEEE Trans. Power Electron.*, vol. 36, no. 7, pp. 7832–7840, 2021.

[4] D. Yang, X. Ruan, and H. Wu, "Impedance shaping of the grid-connected inverter with LCL filter to improve its adaptability to the weak grid condition," *IEEE Trans. Power Electron.*, vol. 29, no. 11, pp. 5795–5805, 2014.

[5] C. Xie, K. Li, J. Zou, D. Liu, and J. M. Guerrero, "Passivity-based design of grid-side current-controlled LCL-type grid-connected inverters," *IEEE Trans. Power Electron.*, vol. 35, no. 9, pp. 9813–9823, 2020.

[6] X. Wang, C. Bao, X. Ruan, W. Li, and D. Pan, "Design considerations of digitally controlled LCL-filtered inverter with capacitor- current-feedback active damping," *IEEE J. Emerg. Sel. Topics Power Electron.*, vol. 2, no. 4, pp. 972–984, 2014.

[7] X. Wang, F. Blaabjerg, and P. C. Loh, "Grid-current-feedback active damping for LCL resonance in grid-connected voltage-source converters," *IEEE Trans. Power Electron*, vol. 31, no. 1, pp. 213–223, 2016.

[8] X. Zhou, L. Zhou, Y. Chen, Z. Shuai, J. M. Guerrero, A. Luo, W. Wu, and L. Yang, "Robust grid-current-feedback resonance suppression method for LCL-type grid-connected inverter connected to weak grid," *IEEE J. Emerg. Sel. Topics Power Electron.*, vol. 6, no. 4, pp. 2126–2137, 2018.

[9] T. Fang, S. Shen, L. Zhang, Y. Jin, and C. Huang, "Capacitor current feedback with phase-lead compensator to eliminate resonant frequency forbidden region for LCL-type grid-connected inverter in weak grid," *IEEE J. Emerg. Sel. Topics Power Electron.*, vol. 9, no. 5, pp. 5581–5596, 2021.

[10] C. Li, Q. Zhang, R. Zhu, F. Deng, J. Zhang, H. Yang, and X. Sun, "Design and analysis of high-frequency phase compensation strategies for CCF-controlled LCL filter-based grid-connected converter," *IEEE J. Emerg. Sel. Topics Power Electron.*, vol. 13, no. 6, pp. 7952–7966, 2025.

[11] C. Li, C. Xie, G. Ma, C. Peng, and J. Zou, "Passivity and injection current quality enhancement for single inverter-side current feedback LCL-type grid-following inverters," *IEEE J. Emerg. Sel. Topics Power Electron.*, vol. 13, no. 2, pp. 2500–2511, 2025.

[12] B. Wen, D. Boroyevich, R. Burgos, P. Mattavelli, and Z. Shen, "Analysis of D-Q small-signal impedance of grid-tied inverters," *IEEE Trans. Power Electron.*, vol. 31, no. 1, pp. 675–687, 2016.

[13] J. Fang, X. Li, H. Li, and Y. Tang, "Stability improvement for three-phase grid-connected converters through impedance reshaping in quadrature-axis," *IEEE Trans. Power Electron.*, vol. 33, no. 10, pp. 8365–8375, 2018.

[14] D. Zhu, S. Zhou, X. Zou, and Y. Kang, "Improved design of PLL controller for LCL-type grid-connected converter in weak grid," *IEEE Trans. Power Electron.*, vol. 35, no. 5, pp. 4715–4727, 2020.

[15] S. Zhou, X. Zou, D. Zhu, L. Tong, Y. Zhao, Y. Kang, and X. Yuan, "An improved design of current controller for LCL-type grid-connected converter to reduce negative effect of PLL in weak grid," *IEEE J. Emerg. Sel. Topics Power Electron.*, vol. 6, no. 2, pp. 648–663, 2018.

[16] H. Gong, X. Wang, and L. Harnefors, "Rethinking current controller design for PLL-synchronized VSCs in weak grids," *IEEE Trans. Power Electron.*, vol. 37, no. 2, pp. 1369–1381, 2022.

[17] S. G. Parker, B. P. McGrath, and D. G. Holmes, "Regions of active damping control for LCL filters," *IEEE Trans. Ind. Appl.*, vol. 50, no. 1, pp. 424–432, 2014.

[18] D. G. Holmes, T. A. Lipo, B. P. McGrath, and W. Y. Kong, "Optimized design of stationary frame three phase AC current regulators," *IEEE Trans. Power Electron.*, vol. 24, no. 11, pp. 2417–2426, 2009.

[19] Z. Xin, P. Mattavelli, W. Yao, Y. Yang, F. Blaabjerg, and P. C. Loh, "Mitigation of grid-current distortion for LCL-filtered voltage-source inverter with inverter-current feedback control," *IEEE Trans. Power Electron.*, vol. 33, no. 7, pp. 6248–6261, 2018.

[20] G. F. Franklin, J. D. Powell, and A. Emami-Naeini, *Feedback Control of Dynamic Systems*, 8th ed. New York, NY: Pearson, 2019.

[21] A. A. Nazib, D. G. Holmes, and B. P. McGrath, "Self-synchronizing stationary frame inverter-current-feedback control for LCL grid-connected inverters," *IEEE J. Emerg. Sel. Topics Power Electron.*, vol. 10, no. 2, pp. 1434–1446, 2022.